

# Calibration-free SH guided wave analysis for screening of wall thickness in steel with varying properties

O. Trushkevych<sup>a</sup>, S. Dixon<sup>a</sup>, M. Tabatabaeipour<sup>b</sup>, M.D.G. Potter<sup>a</sup>, C. MacLeod<sup>b</sup>, G. Dobie<sup>b</sup>, R.S. Edwards<sup>a,\*</sup>

<sup>a</sup> Department of Physics, University of Warwick, Coventry CV4 7AL, United Kingdom

<sup>b</sup> Department of Electronic and Electrical Engineering, University of Strathclyde, Glasgow G11XW, United Kingdom

## ARTICLE INFO

### Keywords:

Ultrasonics  
EMATs  
SH waves  
Defect characterisation

## ABSTRACT

Guided shear horizontal (SH) ultrasonic wavemodes show promise for fast screening of wall thinning and other defects, with miniaturised electromagnetic acoustic transducers (EMATs) offering the potential for automated robotic inspection. However, the use of guided waves for full defect characterisation is strongly affected by mode conversions, changes in lift-off from the sample, variations in material properties and other effects, and these are not typically considered when reporting laboratory results. We show that these factors can have a significant effect on the data as one moves towards industrial implementation, but that a combination of different analysis methods on the SH<sub>0</sub> and SH<sub>1</sub> wavemodes can offer a high reliability of detection, and mitigate some of the issues with changes in experimental conditions and mode conversions. For inspection of 10 mm thick steel plates, the proposed processing of the signals is shown to reliably detect 40 mm diameter flat bottomed holes with 5%–50% wall loss. A rough, approximately 20 × 20 mm square defect with up to 20% wall loss is also detected.

## 1. Introduction

Non-destructive testing (NDT) is critically important for monitoring the condition and safety of vessels, pipelines and storage tanks, to prevent dangerous failures and costly outages [1]. Mounting testing equipment on a robot and automating NDT is extremely attractive as it facilitates access to hazardous environments and allows remote operation [2]. A typical inspection process uses point-by-point scanning, for example using ultrasound bulk waves to measure the thickness at every location, which is slow and may not be suitable for samples with complex geometry [3,4]. Instead, guided waves such as Lamb waves and shear horizontal (SH) waves in plates, and torsional waves in pipes, can be used for defect detection and sizing [4,5].

Most early studies aimed at improving inspection capabilities using guided waves have focused on detection, rather than quantitative sizing, of defects, including corrosion (wall thinning) and cracks. For example, Zhu et al. detected corrosion with 5–20% wall thickness loss and 10 mm lateral dimensions on thin aluminium plates for the A<sub>2</sub> and S<sub>2</sub> Lamb wavemodes [6]. Petcher et al. demonstrated defect detection in welds (e.g. centreline, lack of fusion, wall crack, toe crack) using SH waves generated using electromagnetic acoustic transducers (EMATs), which performed better than a 1D piezoelectric phased array using the total focusing method (TFM) [7].

Recent work has focused on detecting wall thinning in pipes, in particular in inaccessible locations such as under supports. Guided waves behave slightly differently in pipes compared to plates, with all guided wavemodes being dispersive [7]. However, most approaches to detecting wall thinning apply similarly to pipes and plates. Andruschak et al. focused on corrosion at pipe supports and used the dispersive SH<sub>1</sub> mode in the “knee” region of the dispersion curve [8]. The study used SH<sub>1</sub> mode amplitudes and arrival times to identify the presence of a defect. They considered very gradual wall thinning of 10%–25% and observed high-pass frequency filtering of the SH<sub>1</sub> wave-mode propagating through regions with thickness just below the SH<sub>1</sub> mode cut-off thickness, which may have been due to mode conversion. Khalili used the SH<sub>1</sub> mode in the same region for detection of very shallow defects (< 10% cross-sectional thickness loss). Clough et al. used circumferential guided SH waves in pipes to screen for defects and categorised defects into severe and not severe using changes in amplitude and arrival times of the SH<sub>1</sub> mode [9]. They found that, even if the remaining thickness was above the cut-off for the SH<sub>1</sub> mode, it still affected the amplitude.

Recently, much research has focused on quantitative evaluation of defects using SH waves. Howard modelled defect detection probabilities in 10 mm thick steel pipes, using the S<sub>0</sub> Lamb wave-mode and a

\* Corresponding author.

E-mail address: [r.s.edwards@warwick.ac.uk](mailto:r.s.edwards@warwick.ac.uk) (R.S. Edwards).

combined measurement where the SH0 mode was used in reflection and SH1 in transmission for gauging defect lateral dimensions as well as depth [10]. Their modelling used traditional periodic permanent magnet (PPM) SH wave EMAT designs with a 13 mm wavelength, and concluded that defects can be reliably detected when their diameters are equal to or larger than  $1.5\lambda$  with 5 mm depth (50% wall loss), with no sensitivity below that diameter. They also predicted detection of defects with depths 2 mm and deeper when the defect diameter was  $2.5 - 3\lambda$ , with the wavelength resolution dependent on system-specific signal-to-noise ratio (SNR). Attempts to extract remaining thickness of a defect have also been made using the cut-off frequencies of SH waves [11,12]. A high technology readiness level study was reported by Lissenden et al. where SH waves were used to detect semi-circular crack-like defects in mock-up nuclear fuel containers made of 15.9 mm thick stainless steel [13,14]. Lift-off was minimised by using a spring load mechanism. Defects of radius  $> 5.3$  mm were reliably detected, while defects with smaller radii were detected in 50% of cases. The decisions were not automated, and B-scans and operator judgement were used for detection.

There are many factors which could affect the measurements when done in a more realistic environment. No one paper can look at the full parameter space, but the following are considered here: lift-off of EMATs from the sample due to e.g. rough surfaces or coating thickness variations, variations in material properties, and mode conversions at a defect. Each of these factors can cause a change in signal intensity, wave arrival time, and frequency content. In the majority of the literature, it is assumed that these remain constant. Where EMATs are used, lift-off variations will affect the wave amplitude and can also affect the arrival time and frequency content of the measured signal [15]. Changes in material properties during a scan can also change the amplitude, for example by leading to enhanced magnetostrictive generation [16]. Where the detection transducer is wider than the defect, a large proportion of the detected signal will travel past the defect without being affected [17]. Taken together, all of these factors mean that full defect characterisation is very challenging in more realistic scan situations, and realistic defects may be missed or misclassified as insignificant, or false positives may be found. The information collected from a single analysis method, e.g. only the mode arrival time or amplitude, is insufficient to build the defect profile.

In addition, mode conversions between SH modes or into other guided wave modes may be present, and are related to defect geometry [18]. Mode conversions at defect edges were dismissed as insignificant for defects with gradual wall thinning [12,18]. However, they also arise in wedges, even when the length of the wedge is larger than the inspection wavelength [19–21]. The SH1 mode can mode-convert to the SH0 mode in the region of the defect, which can potentially mode convert back again at the other edge of the defect. The SH0 mode can also be converted into the SH1 mode at sharp defects [18]. Mode conversions will affect the frequency content, arrival times and amplitudes of each mode in a complex way, related to defect shape and profile.

Therefore it is not always possible to extract remaining wall thickness information with any reliability. The studies discussed in the previous paragraphs, whether using models or experiments, often report high reliability of detection and/or accuracy of sizing of defects. Typically they will use a simple material, e.g. aluminium, or carefully control material properties (including sample flatness) and EMAT lift-off. However, they do not consider the many mechanisms which will affect measurement of wave amplitude and arrival time in a realistic scanning situation, and which could lead to problems with the reliability of the analysis; particularly where a single analysis method is relied upon, such as variations in wave arrival time.

The variations are such that no analysis method will be perfect in all situations. This paper discusses different methods of defect detection and severity assessment, and how to automate detection of defects by using a combination of measurements together, to overcome many

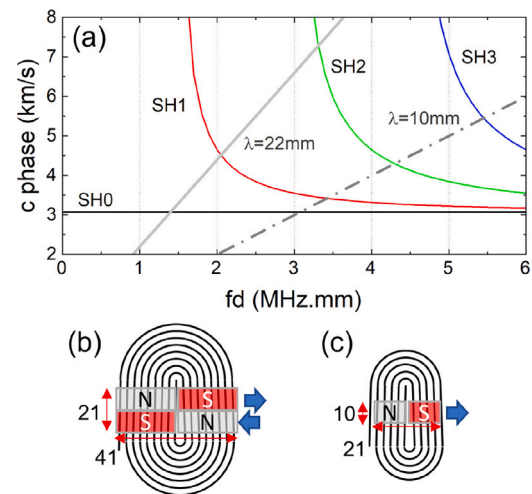


Fig. 1. (a) Dispersion curve for 10 mm thick steel, showing lines of constant wavelength for  $\lambda = 10$  and 22 mm. (b) Directional miniaturised EMAT generator and (c) miniaturised EMAT detector designs for operation at a wavelength of 22 mm.

of the difficulties discussed above. This is not intended to be a full solution—but aims to improve the understanding of the limitations of the methods and suggest ways to improve reliability in a real scan. We argue that frequency filtering and similar measurements, as reported in the literature for laboratory-based studies, should not be over-interpreted, and that detection and classification of defects is more complex than is often perceived.

## 2. Methodology

The experiments are done using miniaturised EMATs that are suitable for deployment on small robotic crawlers, for later automation of the process. EMATs were used to generate and detect SH waves in 10 mm thick steel plates, chosen to mimic steel storage tanks, with their phase velocity shown in Fig. 1(a), plotted against the frequency · thickness product in MHz · mm. Straight lines indicate mode crossing points for two different wavelengths. The EMATs were miniaturised (as described in Ref. [22]) and are a variation on a traditional PPM SH wave EMAT design [23], but with fewer magnets, with typical designs shown in Fig. 1(b) and (c). Reduction of the magnet volume leads to lower signal to noise ratio and poorer signal quality, wider bandwidth and some loss of frequency selectivity, but enables much simpler scanning of ferromagnetic samples where there is significant attraction of the EMAT magnets to the sample. Additionally there is improved spatial resolution when scanning, and higher sensitivity to defects with small lateral dimensions [17,22,24].

Magnet size defines the wavelength, similarly to the PPM design for Lorentz-force SH-wave generation, with this design being standard for inspection of both magnetic and non-magnetic samples. One pair of EMATs was designed to generate and detect a nominal wavelength of 22 mm, and another pair was made to work at a nominal wavelength of 10 mm, with the wavelengths marked as straight lines on the dispersion curve in Fig. 1(a). The 22 mm wavelength generator had four magnets in a periodic array, and was 41 mm wide. The 22 mm wavelength detector had one row of two magnets, with the front being 21 mm wide. The 10 mm wavelength EMATs used more magnets compared to the 22 mm wavelength EMAT, to compensate for the reduced magnet array volume: 6 magnets for the generator and 4 magnets for the detector. Both generator and detector with 10 mm wavelength were 21 mm wide. The drag force of the 10 mm wavelength EMAT pair was lower than that of the 22 mm wavelength pair, and both sets were suitable for robotic inspection using a small crawler robot such

**Table 1**

Optimal frequencies for generating SH0 and SH1 and cut-off thickness of SH1 for 10 mm thick sample for two wavelengths. Note the calculation was done for  $c_s = 3075$  m/s which is the nominal speed for steel; measurements showed this to be different in the samples used.

Wavelength	Calc. SH0 freq.	Calc. SH1 freq.	Expt. SH1 freq.	SH1 cut-off thickness
10 mm	310 kHz	340 kHz	320 kHz	5.1 mm
22 mm	140 kHz	205 kHz	200 kHz	7.7 mm

as the Inuktun Micromag [25]. It was not possible to do scans using commercial EMATs due to the strength of the magnetic attraction and drag force.

A set of steel samples of thickness 10 mm and with lateral dimensions  $0.3 \times 1$  m were produced, each containing a set of flat bottomed holes (FBH) of 40 mm diameter. FBH depths were 0.5, 1, 1.5, 2, 2.5, 3 and 5 mm, to simulate shallow defects with 50%–95% remaining wall thickness. A further sample of dimensions  $1.5 \times 1.5$  m with an uneven corrosion layer was also tested. The corrosion layer contained magnetite which is known to affect the amplitude of EMAT generation. This sample contained a hand-made defect with  $20 \times 20$  mm side lengths and an uneven depth with a maximum value of 2 mm. This sample and defect were used as a more realistic challenge for defect detection.

A “low” frequency RITEC Pulser/ Receiver RPR4000 was used to drive the generation EMATs, using either 3 or 10 cycles for the 22 mm wavelength EMAT at 200 kHz. Three cycle excitation at 320 kHz was used to drive the EMATs with 10 mm wavelength. The excitation frequency was chosen to generate the SH1 mode efficiently [26,27]. To ensure that Fig. 1(a) was accurate, the speed of the SH0 wave was first measured for both sets of samples by gradually increasing separation between the generation and detection EMATs and measuring arrival times. This enables a measurement to be obtained without errors due to electronic delays in the equipment. For the 0.3 m wide plates the velocity was  $3084 \pm 8$  m/s. The large plate exhibited a slight anisotropy of shear speed in the  $x$  and  $y$  directions, with values of  $3081 \pm 6$  m/s and  $3096 \pm 6$  m/s.

The two wavelengths of SH guided waves were chosen to study the influence of the wavelength on defect detection capabilities, in particular in the context of miniaturised transducers, which are more broadband compared to commercially available EMATs [27]. When choosing the wavelength, the following should be taken into account:

- lift-off tolerance (longer wavelength gives improved lift-off behaviour)
- sample size (longer wavelength requires a larger distance between transducers)
- lateral defect size (defects with smaller area will be more likely to be detected by shorter wavelengths and smaller transducers)
- defect depth of interest (longer wavelengths may be more sensitive to wall thinning; the line for  $\lambda = 22$  mm in Fig. 1(a) crosses the dispersion curve for SH1 at a region where it is highly sensitive to changes in the frequency-thickness product  $fd$ , while SH1 for 10 mm wavelength will be less sensitive to thickness change).

From the dispersion relation of SH waves in a plate, the cut-off frequency thickness ( $fd$ ) is given by

$$(fd)_n^{cut\ off} = (nc_s)/2, \quad (1)$$

where  $n$  is the order of the mode and  $c_s$  is the shear wave speed [21]. In 10 mm thick plate, this leads to a minimum thickness at which the SH1 wavemode can still propagate (the cut-off thickness) of 5.1 mm for  $\lambda = 10$  mm, and 7.7 mm for  $\lambda = 22$  mm. The experimentally obtained optimal generation frequency, found by looking for the maximum amplitude signal, is given in Table 1, and differed slightly from the calculated value due to the transducers being handmade and the wavelength not being exact. The same frequencies were used for all measurements.

SH waves were sent between a generator and detector EMAT in pitch-catch mode. The EMATs were mounted into a roller, providing

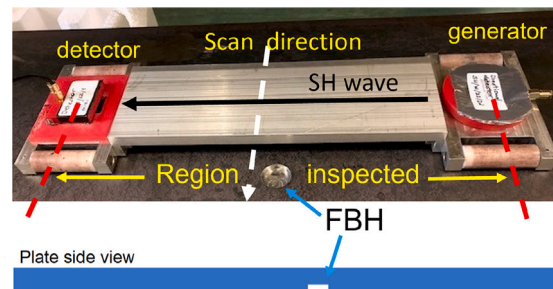


Fig. 2. Setup with generating and detecting EMATs in pitch-catch configuration performing a line scan.

ease of movement and fixed separation of 0.3 m between transducers (Fig. 2), chosen due to the limitations in sample size and placement of the defects. The lift-off was kept as small as possible but varied due to surface roughness. Scans of the samples were done manually with a 5 mm step size. The defects were positioned on a line approximately in the centre of the generator and detector. Fig. 2 shows a scan in the  $x$ -direction. To perform a second scan in the  $y$ -direction, the EMAT pair was rotated  $90^\circ$  with the scan direction remaining perpendicular to the SH-wave propagation direction. This is beneficial when locating a defect in two-dimensions.

Each scan aimed to highlight any areas with potential defects. The whole area between the transducers is investigated in one measurement, and it is then possible to “zoom-in” to suspected areas by scanning along different paths to narrow down the defect position. The screening results can then be verified by point-by-point thickness measurements in just the flagged areas, significantly speeding up the inspection process.

This paper investigates typical variations in experimental results on industrial samples, highlighting how the use of multiple signal analysis methods and a combination of the results can give reliable detection, whereas using just a single analysis method would be significantly prone to false positives and missed or mis-classified defects. This paper considers the following analysis methods:

- SH0 and SH1 amplitudes, and their relative changes with lift-off
- A suitable combination of SH0 and SH1 amplitudes, in order to reduce the lift-off variation
- Mode arrival times
- Frequency measurements and optimal SH wavelength
- Combinations of these measurements to improve reliability.

Here we explore how these and other parameters could be used to yield a fast, reliable method of defect screening using robotic inspection-compatible EMATs, with improved probability of detection by combining results together using data fusion.

### 3. Results and discussion

For defect detection using guided waves, one can use the amplitude or the transmission and reflection coefficients of particular modes [13, 21,28]. Arrival times [9] and frequency content [29] have also been used. Each of these measurements may be subject to errors.

Typical signals for 200 kHz,  $\lambda = 22$  mm, 3 cycle generation are shown in Fig. 3 for single shot data. Whilst there is significant noise,

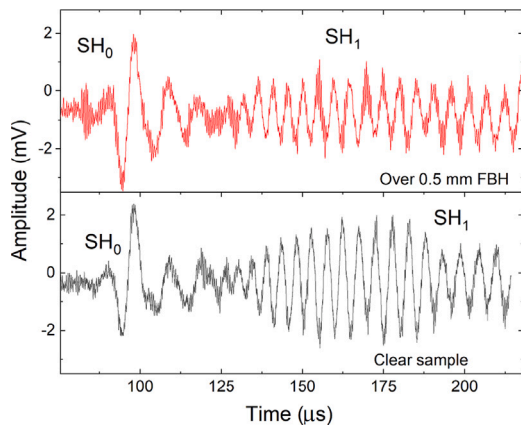


Fig. 3. Typical pitch catch signal obtained with 3 cycles excitation, at a frequency of 200 kHz for  $\lambda = 22$  mm, on a clear sample section and over a 0.5 mm deep, 40 mm diameter FBH.

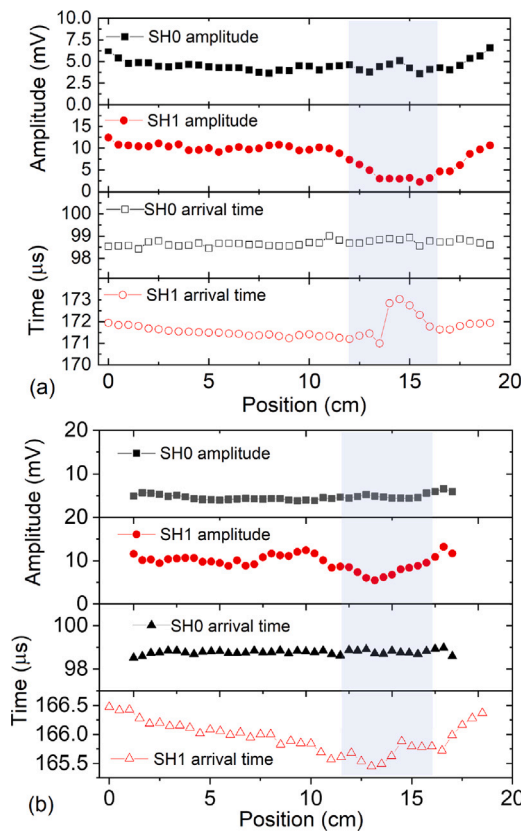


Fig. 4. (a) Results for a 40 mm diameter, 3 mm deep FBH, positioned between 12 and 16 cm on the scan. (b) A similar scan on a 40 mm diameter, 0.5 mm deep FBH. Blue region indicates that the defect is between the EMATs. (For interpretation of the references to colour in this figure legend, the reader is referred to the web version of this article.)

SH0 and SH1 modes are clearly visible. Data is shown for the EMATs above a clear section (black), and over a 40 mm diameter ( $1.8\lambda$ ), 0.5 mm deep FBH (red, 5% wall thickness loss). To quantify typical changes in signal amplitude and arrival time, scans were made across two different FBHs, both 40 mm in diameter; the first 3 mm deep, and the second 0.5 mm deep. SH0 and SH1 mode amplitudes and arrival times are shown in Fig. 4. The blue box shows the position of the defect. Due to the generation EMAT width, a defect is noticeable before it is fully aligned with the centres of the scanning EMATs.

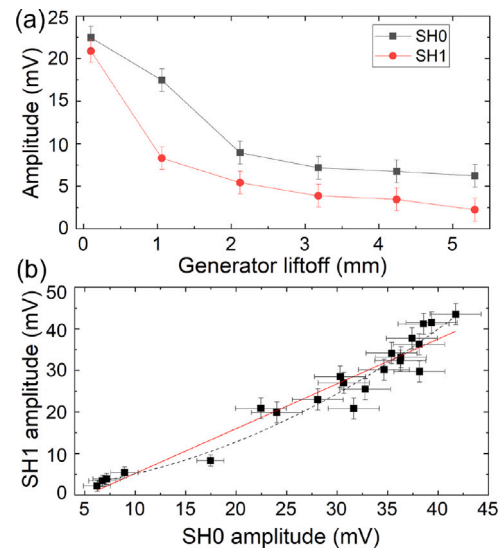


Fig. 5. (a) Lift-off behaviour of amplitudes of SH0 and SH1 wavemodes, for generator lift-off only; (b) generator and detector lift-off measurements represented as a relationship between SH1 and SH0 amplitudes, showing the linear fit (solid line) and polynomial fit (dashed line).

Fig. 4 shows that SH1 mode amplitude is a good indicator of a defect, showing a dip in amplitude in the regions of the defects, while the SH0 mode amplitude remains relatively constant for both defects. The slight increase in SH0 mode amplitude at the beginning and end of the scans is due to edge effects. Similarly, the arrival time of the SH0 mode shows limited variations, while the SH1 mode shows some variation—however, the variation behaviour is not the same for each defect. This scan was done very carefully on a smooth-surface sample, ensuring that there were no significant material variations and that lift-off remained constant—without these considerations both amplitudes would show variations due to the changes, as well as any variations due to defects.

### 3.1. Amplitude behaviour with EMAT lift-off

When scanning real samples, lift-off and material property variations are inevitable. They may be due to paint thickness variations, corrosion on the surface, or varying surface roughness. They can lead to a change in signal intensity, arrival times and frequency content [30, 31]. Ideally, lift-off variations should be minimised through system design [13]. However, this is not always possible on rough or rusty surfaces.

Fig. 5(a) shows the amplitudes of the SH0 and SH1 modes when generator lift-off is varied from 0.1 to 5.2 mm, with the detector at a fixed small lift-off. Both modes show a drop-off in amplitude with lift-off. Error bars were calculated using the measurement uncertainty due to noise levels in each measurement. Fig. 5(b) shows data from an experiment where the generator lift-off was varied from 0.1–0.52 mm and detector lift-off was varied from 0 to 0.3 mm, plotting SH1 mode amplitude vs. SH0 mode amplitude for each measurement. The SH0 and SH1 wavemodes have different frequencies for the same wavelength, and lift-off affects higher frequencies more. However, over this range the variation can be fitted to a linear fit (parameters  $1.07725x - 0.00555$ ), or a polynomial fit (parameters  $0.00134 + 0.18202x + 19.57407x^2$ ), where  $x$  is SH0 amplitude. The exact fit is applicable for the sample under test and the EMAT designs used; however very similar relationships have been found for the different samples investigated experimentally in this report.

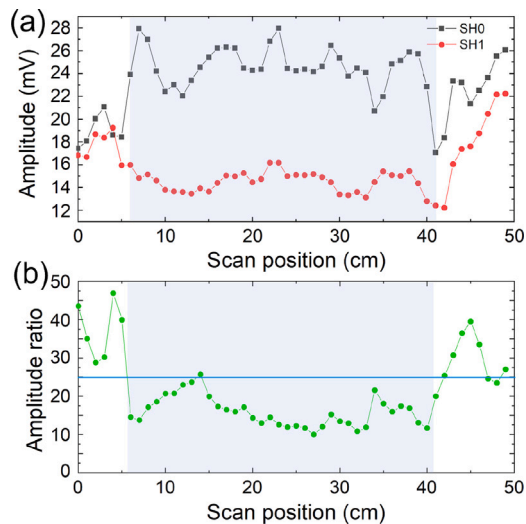


Fig. 6. Scans of large steel sample, moving from having both EMATs one side of the defect, to both on the opposite side of the defect. (a) shows the SH0 and SH1 amplitudes separately, while (b) shows the ratio SH1/SH0. Blue region indicates that the defect is between the EMATs. (For interpretation of the references to colour in this figure legend, the reader is referred to the web version of this article.)

### 3.2. SH1 and SH0 amplitude behaviour

Fig. 6(a) shows measurements made on the large steel sample with the machined defect, which was rough and had rust in patches on the surface, leading to variations in lift-off and material properties during the scan. The EMATs were placed in the roller and scanned from being both on one side of the defect, to a set of positions where the defect was somewhere in-between the EMATs (shown by the grey region), to both being on the opposite side of the defect (scan direction orthogonal to that shown in Fig. 2). There is some variation in both the SH0 and SH1 mode amplitudes during the scan, with this particularly clear for the SH0 mode. Additionally, signal amplitudes when the EMATs were both on the left side of the defect were significantly different to the amplitudes when they were both on the right side of the defect, showing that just using wave amplitude of a single wavemode is not suitable where there may be changes in lift-off and/or in material composition (thickness of corrosion layer) underneath the EMATs.

A near-linear dependence between the mode amplitudes with lift-off allows the use of the SH0 mode amplitude as a reference to minimise lift-off dependence. This could be either by taking the ratio between SH1 and SH0 mode amplitudes (shown in Fig. 6(b)), or, for small variations in lift-off and material properties, by taking the difference between the SH1 and SH0 mode amplitudes (safer where SH0 mode amplitudes are low and may approach zero). For the ratio measurement shown here it is possible to see a clear drop in relative amplitude when the defect is present, significantly larger than any variation with position away from the defect edges.

Fig. 7 shows the amplitude difference (SH1-SH0) and amplitude ratio (SH1/SH0) for scans over the samples containing 40 mm diameter FBH defects. Excitation using 3 and 10 cycles of drive current are compared; 10 cycles will give a more narrowband signal optimised for SH1 mode generation, allowing better use of the SH1 mode cut-off. The shaded region shows the approximate defect position for each scan.

Each graph shows a clear dip in the region of the defect even for the 0.5 mm deep defect. The 10 cycle excitation gives clearer results with lower noise levels, which may be due to the higher SH1 mode amplitude. The depth of a defect that should cut-off the SH1 mode was calculated to be about 2.3 mm (remaining wall thickness of 7.7 mm, Table 1). However, even the thinnest FBH with only 5% reduction of

thickness is clearly distinguishable from the undamaged area scan. All FBH with depths of 1 mm and greater have very similar behaviour to that observed in Fig. 7.

This data shows the problem with considering only the change in amplitude of a wave mode to size defects, even if lift-off is taken into consideration. The behaviour gives an indication of a defect, but there is no simple method for gauging defect size and width. For severe defects with sharp features, the SH0 mode amplitude is also affected, and comparisons of the SH1 and SH0 amplitudes may no longer be a reliable parameter.

### 3.3. Mode arrival times

Arrival times have previously been suggested as an indicator of a defect or as a method to measure its geometry. As the frequency-thickness product ( $fd$ ) changes, the velocity of each mode of higher order than the SH0 mode also changes, leading to a change in arrival time. This measurement is particularly effective where  $fd$  means that the velocity is in a highly dispersive region. However, the assumption of how arrival time changes does not take into account mode conversion, which can affect arrival time in the opposite manner due to the difference in speeds of the SH0 and SH1 modes. SH0 and SH1 mode arrival times are also sensitive to lift-off variations due to the changing effective footprint of the EMAT on the sample, but the amplitude of the associated changes is only small, around  $0.1 \mu\text{s}$  [15].

To calculate SH0 and SH1 mode arrival times, a chosen peak in the cycle near the centre of the wave envelope is windowed and tracked throughout the scan, measuring changes due to phase velocity variations. Here, a change in  $fd$  will lead to a larger velocity for the SH1 mode and hence an earlier arrival time, and this mechanism is expected to dominate for shallower defects away from the cut-off. Where there is mode conversion to SH0, the reduced phase velocity means there will be a contribution which causes waves to be delayed, along with interference between the two modes if the SH1 mode is still present [18].

Fig. 8 shows the arrival times for the SH0 and SH1 modes for scans over a clear area and over multiple 40 mm diameter FBHs, for 10 cycle drive current excitation. A gradual increase in arrival times towards the beginning and end of all scans is due to edge effects. The SH0 mode arrival times show no consistent variations.

We observe that the SH1 mode arrival times decrease for shallower defects and increase for FBHs of 1.5 mm and deeper, as expected. For severe defects where mode conversions are significant, analysis is complex and it is difficult to track the peaks in the signal, leading to artifacts in arrival times, e.g. the 5 mm deep FBH. Changes in SH1 mode arrival time are noticeable even for the thinnest of the defects.

For defect detection, rather than using absolute changes above a threshold, it is more practical to use deviation (whether positive or negative) of SH1 mode arrival time in conjunction with amplitude measurements as a marker for possible defect. Sizing faces challenges, as the defect geometry can lead to different levels of mode conversion and hence affect the arrival times differently [18].

### 3.4. Frequency measurements

The frequency measured during experiments is a property of the generation frequency from the pulser (including number of cycles chosen), any filtering of frequencies within the sample (e.g. cut-off frequency and mode conversions), the sample properties, and the lift-off of the EMAT above the sample [15,31]. The smaller the number of cycles, the more broadband the signal will be.

The frequency behaviour has been analysed in two ways. Firstly, the central frequency was extracted by finding the frequency corresponding to the maximum in the fast Fourier transform (FFT) of the time signals shown in Fig. 3. Where the thickness is close to the cut-off value of  $fd$ , lower frequencies in the SH1 mode will be filtered out [8] and the

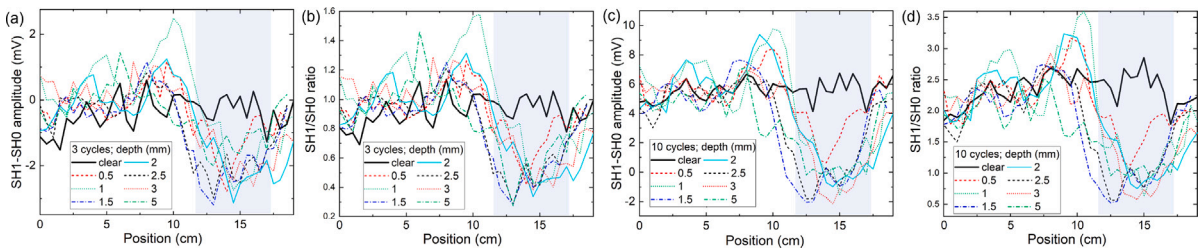


Fig. 7. Scan over a clear area and over areas with 40 mm diameter flat bottomed holes of varying depth (given in the legend). 3 cycles excitation showing (a) SH1-SH0, (b) SH1/SH0; 10 cycles excitation showing (c) SH1-SH0, (d) SH1/SH0.

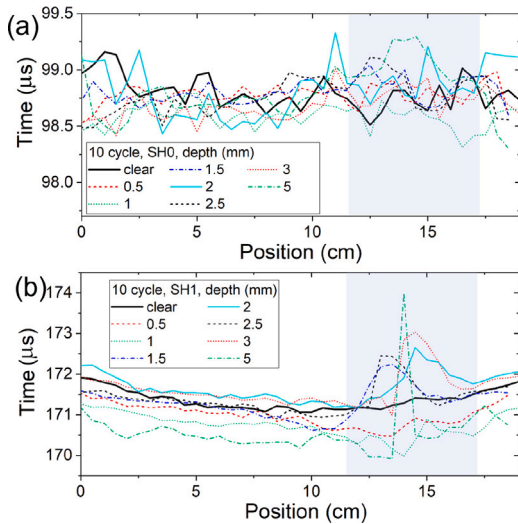


Fig. 8. Arrival times of (a) SH0 and (b) SH1 for scans over 40 mm FBH with varying thickness, with a clear area scan shown for comparison. 10 cycle excitation. Blue region again shows where the defect is between the EMATs. (For interpretation of the references to colour in this figure legend, the reader is referred to the web version of this article.)

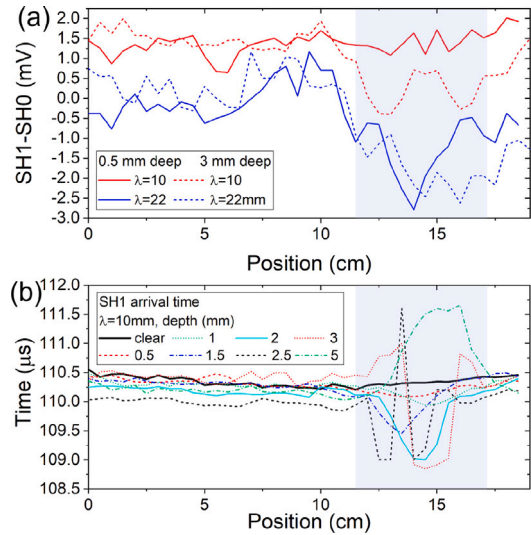


Fig. 10. (a) Dependence of SH1-SH0 amplitude measurement on wavelength, shown for two FBH depths and two wavelengths. (b) SH1 arrival time variations for 10 mm wavelength.

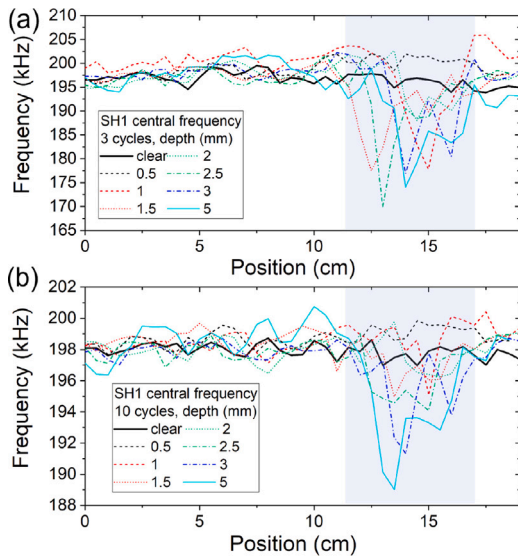


Fig. 9. Central frequency from FFT for (a) 3 cycle and (b) 10 cycle excitation, 22 mm wavelength.

central frequency will shift to higher values in the absence of mode conversions. However, mode conversion will again complicate matters and give a defect geometry-dependent behaviour [19,20]. Lift-off changes would lead to a small reduction in frequency of the signal [15].

Fig. 9 shows how this parameter is affected by wall thinning. In all cases, the frequency goes down rather than up where a defect is present. For 3 cycle excitation (more broadband) all defects of depth 1 mm and above can be observed by looking for a reduction. For 10 cycle excitation, changes in the central frequency of the mode can be reliably observed for 2.5 mm FBH and deeper. The decrease in frequency can be explained by mode conversions; firstly from SH0 to SH1 at defect edges, which will lead to an increased presence of lower frequencies because the frequency of the SH0 mode (around 100 kHz for 22 mm wavelength) does not change upon conversion, and the close arrival times of the two modes means that there will be some contribution from this mode in the window chosen [19,20]. In addition, as the SH1 mode amplitude is reduced due to a defect, the SH0 mode contribution to the frequency spectrum increases, reducing the overall frequency.

### 3.5. Wavelength comparison

The performance of 10 mm wavelength EMATs was also evaluated for defect detection. Smaller wavelength SH wave EMATs have a naturally smaller magnetic drag due to a smaller size of magnets, therefore they are good contenders for mounting on a robot. However, they suffer more from lift-off variations, and are less sensitive to wall thinning due to the different position on the dispersion curve. There is less flexibility over the number of cycles of excitation, because on 10 mm thick steel

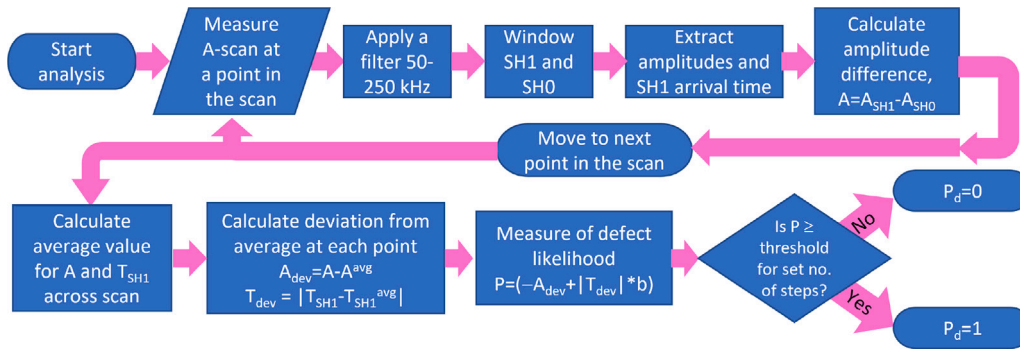


Fig. 11. Data processing steps combining SH0, SH1 amplitudes and arrival times into defect likelihood measure for defect detection. Note that scan end-point is not included in this diagram.

the SH0 and SH1 modes have a small difference in propagation speed, and cannot be easily separated when 10 cycle excitation is used; hence 3 cycle excitation was used for these measurements.

Fig. 10(a) illustrates the differences between scans over two defects using 10 mm and 22 mm wavelengths. The thinnest defect can be detected from amplitude analysis alone for  $\lambda = 22$  mm, but is not observed in the amplitude data for  $\lambda = 10$  mm, as expected. For  $\lambda = 10$  mm, changes in SH1-SH0 amplitudes are observed for defects 1.5 mm and deeper. Once the changes are observed, their amplitude does not correlate with the defect depth. Fig. 10(b) shows SH1 mode arrival times for  $\lambda = 10$  mm inspection for all FBHs. Measurements showed that the arrival time decreased for all FBH except the 5 mm deep defect, which is below the cut-off thickness for the SH1 mode at this wavelength. Different inspection wavelengths have different sensitivity to defects, but choice of wavelength should be made with care as there will be a large uncertainty due to the unknown defect size and thickness profile. Overall, measurements using 22 mm wavelength were more robust, with higher SNR and smaller variations due to lift-off sensitivity, and clear separation into SH0 and SH1 wavemodes.

#### 4. Defect detection - constructing a defect classification measure

Several measured parameters were combined into a measurement of defect likelihood and classification into defect/no defect, and a defect was indicated where a user-defined threshold was reached for multiple parameters over a minimum scan width, chosen to remove the chance of noise effects dominating the classification. For these measurements the minimum width was set to 4 scan steps (20 mm scan distance), which was the width of the detection EMAT; this is the expected minimum size that any defect would appear to be in a scan as the transducer pair is scanned over it [17]. The threshold on each parameter was chosen to minimise false positives on a clear area, while still being sensitive to defects when scanning the smooth samples containing FBHs. The same data processing and thresholds were applied to all data from scans.

The diagram in Fig. 11 shows how measured parameters were combined into a measure of defect likelihood for defect detection when considering just amplitude and arrival times (a limited choice shown for simplicity). Other parameters discussed above could also be included: e.g. SH0 mode arrival times or central frequency of the SH1 wavemode.

The processing first applied a 2nd order Butterworth bandpass filter to the data to reduce noise. Windowing of the modes depends on the number of cycles of excitation and distance between the transducers and was set up manually at the beginning of the processing for a specific EMAT arrangement. For this simple version of the analysis, at each position the amplitudes of the SH0 and SH1 modes, the amplitude difference  $A = A_{SH1} - A_{SH0}$ , and the arrival time of the SH1 mode ( $T_{SH1}$ ) were measured. Then, once these were extracted for all points in

the scan, the following processing steps were taken. For more complex systems, other factors could be added.

Firstly, the average values of  $A$  and  $T_{SH1}$  were calculated across the whole scan, including intact regions and defective regions. This allowed measurement of the deviation from average values at each point, and enabled normalisation so that the same threshold could be applied regardless of sample or transducer changes. The deviation from average at each point was calculated as

$$A_{dev} = A - A^{avg}$$

$$T_{dev} = |T_{SH1} - T_{SH1}^{avg}| \quad (2)$$

Then, a defect likelihood parameter was calculated using

$$P = (-A_{dev} + |T_{dev}| \times b), \quad (3)$$

where the equation was defined by studying the combination which gave the most reliable value. The weighting coefficient  $b$  adjusted the relative weight of the arrival time and amplitude changes, with values of 10 and 100 tested. Once the combined value was obtained, a maximum value of 1 was set on  $P$  and any values above this were rounded down. A threshold was then applied to define areas with likely defects, with a digital value of  $P_d = 1$  if the conditions are met and a defect is likely to be present, and  $P_d = 0$  otherwise.

The processing can be adapted for specific samples (expected defect size and severity, sample anisotropy), scanning conditions (scan step, transducer size, lift-off variations) and sensitivity requirements by changing threshold level, weighting parameter or choosing a different set of parameters to analyse. For samples with isolated defects, deviations from average values give excellent results without any calibration.

The algorithm in Fig. 11 was tested on all scan data sets, for both values of the weighting coefficient  $b$ . Using the same processing parameters and the  $\lambda = 22$  mm EMATs, all FBHs were detected and a scan over a non-defected area showed no defect indication for both weighting values. For  $\lambda = 10$  mm the 0.5 mm defect was not detected, and the 1 mm deep FBH could only be detected for the larger weighting value. All deeper defects were reliably detected, although for  $b = 10$  some were detected as a defect pair rather than one larger defect. Fig. 12 shows examples of processing results on the 0.5 mm, 1 mm and 3 mm deep FBH using the  $\lambda = 22$  mm EMATs and 10 cycle excitation, for  $b = 10$  and processing described in Fig. 11. All defects are reliably detected and there were no false positives.

Fig. 13 shows scan geometry and processing result for the more realistic, uneven defect on the anisotropic plate with uneven corrosion layer, using the 22 mm wavelength EMATs. In this sample the arrival times for both wavemodes were inconsistent across the scan; speed anisotropy is not sufficient to explain this, and it is attributed to the non-uniform layer of magnetostrictive magnetite existing alongside the corrosion layer. Magnetite has been shown to influence the characteristics of generated wavemodes, leading to additional consideration of

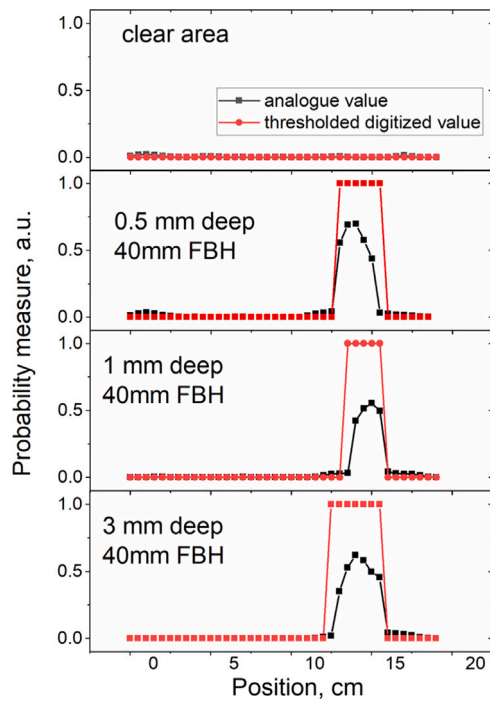


Fig. 12. Fast screening results using the combination of SH0 and SH1 wavemodes and arrival times with weighting  $b = 100$ .

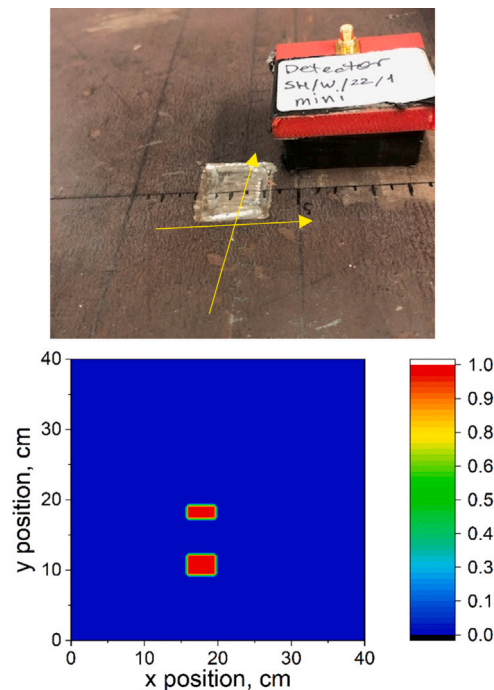


Fig. 13. Geometry of the scans on the large plate, and map constructed from two scans made over the same area in perpendicular directions for  $b = 10$ . (For interpretation of the of the colour scale, the reader is referred to the web version of this article.).

the magnetostrictive generation mechanism [26]. To reduce unwanted noise  $b = 10$  was used, and all other analysis parameters were kept the same as for the FBH scans.

The map was produced from two line scans in the directions shown by the yellow arrows. The defect centre is at the position 17.5 cm in  $x$  and 19.5 cm in  $y$ , and a defect is clearly indicated in this position. There is also a defect indication in the  $y$ -direction at around 10 cm. This

appears for all choices of processing parameters and values of  $b$  tested other than the most restrictive/most likely to miss real defects. Thickness gauging measurements using a shear-bulk-wave EMAT showed a reduction in thickness of around 0.7 mm in the generation region for this scan, and a significant change in birefringence, both of which will significantly affect results. The thickness reduction measured is similar to that of the machined defect, and likely to be partially due to corrosion patches on the hidden side of the plate, and partly due to birefringence issues. Both will affect SH-wave analysis.

The sample has high variability in signal quality due to corrosion, and it is remarkable that even with this background variation, a defect of only  $0.9\lambda$  in size and uneven wall loss of up to 20% is detected, along with detection of corrosion.

### 5. Conclusions

The defect detection capability of miniature SH wave EMATs that are suitable for robotic inspection was studied, and the need to look at multiple parameters to gain a reliable defect location algorithm was highlighted for realistic scans where it is not possible to fully control lift-off, material property changes, and mode conversions. This work demonstrates that previous reports showing high reliability of measurements need to be carefully considered when applying SH waves in industry; however, even a simple combination of analysis parameters can be highly beneficial in improving reliability of detection where the situation is more complex.

Parameters such as amplitudes, arrival times and frequency content, and their combinations were considered for monitoring. No calibration reference on an undamaged area was required where there was some certainty that there were only a small number of defective regions over the scan length. In more complex cases, it would be advisable to take a reference of an undamaged part of the sample and analyse data in reference to that measurement.

Artificial defects (flat bottomed holes) representing 5% to 50% wall thinning with lateral dimensions of 40 mm ( $1.8\lambda$ ) were successfully detected using miniature EMATs with 22 mm wavelength. A realistic uneven square defect with 20 mm ( $0.9\lambda$ ) lateral size and variable thickness up to 2 mm in depth on a plate (with variable rust layer with magnetite presence and anisotropy in shear wave speeds) has also been mapped using two perpendicular line scans covering a square area of  $40 \times 40$  cm. The defect was successfully detected, with an indication of hidden corrosion and significant changes in material properties also observed. The demonstrated EMAT performance compares favourably and even exceeds the modelling prediction of Ref. [10].

It is not possible to reliably extract remaining wall thickness from the described guided wave measurements, despite earlier reports, once mode conversions and experimental variations (e.g. presence of magnetite) are included. Even from this data, with controlled defect profiles we observed very little correlation of parameters with defect depth. In practice, the exact defect position, profile, and size will be unknown, and these parameters play a critical part in transmission and reflection coefficients and mode conversions [20]. However, it was shown that miniaturised EMATs are suitable for defect detection and fast robotic screening of defects. Scans could be made using robotic inspection to highlight areas which were potentially defective, without having to use a time-costly, point-by-point thickness gauging scan. A thickness gauging probe can then be used in specific locations to confirm findings, and may be deployed at regular intervals while screening to improve reliability.

The possibility of defect classification by severity could be done by looking at differences in defect detection sensitivities by two wavelengths, as well as considering SH0 mode arrival time as a measure of the presence of a severe defect. Our further work will investigate using several EMATs with different wavelengths or a tuneable wavelength EMAT. Long wavelengths are more sensitive to wall thinning, and smaller changes in thickness will be picked up, while shorter

wavelengths will be more sensitive to defects with small lateral size. In this way fast screening would be possible, with an ability to categorise defects into several categories, according to their severity and size. This does draw on inspection with different frequencies and wavelengths similar to Ref. [12], but will not rely on the absence of mode conversions.

#### CRedit authorship contribution statement

**O. Trushkevych:** Conceptualisation, Methodology, Validation, Analysis, Investigation, Writing – original draft. **S. Dixon:** Conceptualisation, Supervision, General advice, Writing – review & editing. **M. Tabatabaeipour:** Writing – review & editing, Advice on robotic implementation. **M.D.G. Potter:** Methodology, Assistance in investigation, Writing – review & editing. **C. MacLeod:** Writing – review & editing, Advice on robotic implementation. **G. Dobie:** Funding acquisition, Writing – review & editing, Advice on robotic implementation. **R.S. Edwards:** Conceptualisation, Methodology, Investigation Writing – original draft, Supervision, Project administration, Funding acquisition.

#### Declaration of competing interest

The authors declare that they have no known competing financial interests or personal relationships that could have appeared to influence the work reported in this paper.

#### Data availability

Data will be made available on request.

#### Acknowledgements

The work has been done through RCNDE Core Research funding 2018–20, Remote and Automated Delivery of Non-Contact NDE Sensors. This forms part of the RCNDE funding provided by Engineering and Physical Sciences Research Council and industry, United Kingdom (EP/L022125/1).

#### References

- [1] Zonta D, Glisic B, Adriaenssens S. *Struct Control Health Monit* 2014;21:1043–56.
- [2] Farley JM, Babcock M. Best Practice in NDT applications: an update. In: 16th world conference on NDT (WCNDT 2004), Montreal (Canada). 2004.
- [3] Blyth WA. Robotic pipe inspection: System design, locomotion and control [EngD thesis], Imperial College London; 2017.
- [4] Eddyfi Scorpion 2 manual. 2020, <https://www.eddyfi.com/en/product/scorpion-2> [Accessed 04 2020].
- [5] Rose JL. *Ultrasonic waves in solid media*. Cambridge University Press; 2014.
- [6] Zhu W, Rose JN, Barshinger JN, Agarwala VS. *Res Nondestruct Eval* 1998;10(4):205–25.
- [7] Petcher PA, Dixon SM. *NDT & E Int* 2015;74:58–65.
- [8] Andruschak N, Saletes I, Filletier T, Sinclair A. *NDT & E Int* 2015;75:72–9.
- [9] Clough M, Fleming M, Dixon SM. *NDT & E Int* 2017;86:20–7.
- [10] Howard R, Cegla F. *NDT & E Int* 2017;91:108–19.
- [11] Belanger P. *Ultrasonics* 2014;54:1078–87.
- [12] Suresh N, Balasubramaniam K. *NDT & E Int* 2020;116:102313.
- [13] Cho H, Choi S, Lissenden CJ. *ASME J Nondestruct Eval* 2020;3(2):021001.
- [14] Choi S, Cho H, Lissenden CJ. *Nucl Eng Technol* 2018;50:890–8.
- [15] Xiang L, Dixon S, Thring CB, Li Z, Edwards RS. *NDT & E Int* 2022;126:102576.
- [16] Chikazumi S. *Physics of ferromagnetism*. Oxford University Press; 1997.
- [17] Trushkevych O, Edwards RS. *NDT & E Int* 2019;107:102140.
- [18] Nurmalia H, Nakamura N, Ogi H, Hirao M, Nakahata K. *NDT & E Int* 2012;45:156–61.
- [19] Kubrusly AC, von der Weid JP, Dixon S. *NDT & E Int* 2019;108:102175.
- [20] Kubrusly AC, Freitas MA, von der Weid JP, Dixon SM. *NDT & E Int* 2019;101:94–103.
- [21] Petcher PA, Dixon SM. *Nondestruct Test Eval* 2017;32(2):113–32.
- [22] Trushkevych O, Tabatabaeipour M, Dixon S, Potter MDG, Dobie G, MacLeod C, Edwards RS. *IEEE Sensors* 2021;21(2):1386–94.
- [23] Hirao M, Ogi H. *NDT & E Int* 1999;32(3):127–32.
- [24] Trushkevych O, Edwards RS. *IEEE Sensors J* 2020;1–7, Early Access.
- [25] Inuktun micromag crawler. 2019, <http://inuktun.com/en/products/onsite-standard-products/micromag-miniature-magnetic-crawler/> [Accessed 12 2019].
- [26] Trushkevych O, Dixon SM, Tabatabaeipour M, Dobbie G, Potter MD, MacLeod C, Gachagan A, Pierce SG, Trushkevych O. 2019 IEEE International Ultrasonics Symposium (IUS). 2019. p. 104–7.
- [27] Trushkevych O, Tabatabaeipour M, Dixon S, Potter M, Dobbie G, MacLeod C, Edwards R. *IEEE Sensors* 2021;21(2):1386–94.
- [28] Dobie G, Summan R, Pierce SG, Galbraith W, Hayward G. *IEEE Sens J* 2011;11(10):2458–68.
- [29] Khalili P, Cawley P. *NDT & E Int* 2018;99:80–92.
- [30] Heideklang R. Data fusion for multi-sensor nondestructive detection of surface cracks in ferromagnetic materials [Thesis], Humboldt-Universität zu Berlin; 2018.
- [31] Jian X, Dixon S, Edwards RS, Morrison J. *Ultrasonics* 2006;44:653–6.